

High-speed *in vitro* intensity diffraction tomography

Jiaji Li^{1,2}, Alex Matlock², Yunzhe Li², Qian Chen¹, Chao Zuo^{1,*}, Lei Tian^{2,*}

1. School of Electronic and Optical Engineering, Nanjing University of Science and Technology, No. 200 Xiaolingwei Street, Nanjing, Jiangsu Province 210094, China

2. Department of Electrical and Computer Engineering, Boston University, Boston, MA 02215, USA

Correspondence to: zuocho@njjust.edu.cn, leitian@bu.edu

December 15, 2024

Abstract

We demonstrate a label-free, scan-free intensity diffraction tomography technique utilizing annular illumination (aIDT) to rapidly characterize large-volume 3D refractive index distributions *in vitro*. By optimally matching the illumination geometry to the microscope pupil, our technique reduces the data requirement by $60\times$ to achieve high-speed 10 Hz volume rates. Using 8 intensity images, we recover $\sim 350 \times 100 \times 20\mu\text{m}^3$ volumes with near diffraction-limited lateral resolution of 487 nm and axial resolution of $3.4\mu\text{m}$. Our technique's large volume rate and high resolution enables 3D quantitative phase imaging of complex living biological samples across multiple length scales. We demonstrate aIDT's capabilities on unicellular diatom microalgae, epithelial buccal cell clusters with native bacteria, and live *Caenorhabditis elegans* (*C. elegans*) specimens. Within these samples, we recover macroscale cellular structures, subcellular organelles, and dynamic micro-organism tissues with minimal motion artifacts. Quantifying such features has significant utility in oncology, immunology, and cellular pathophysiology, where these morphological features are evaluated for changes in the presence of disease, parasites, and new drug treatments. aIDT shows promise as a powerful high-speed, label-free microscopy technique for these applications where natural imaging is required to evaluate environmental effects on a sample in real-time.

1 Introduction

Three-dimensional (3D) refractive index (RI) distributions of cells and tissues are useful for the morphological detection and diagnosis of disease in biomedical imaging [1]. For example, characterizing RI distribution has shown particular utility in understanding disease and morphogenesis [2]. Quantitatively characterizing thick biological samples across multiple subcellular and multicellular scales, however, remains a challenging task. Here, we present a scan-free, high-speed intensity diffraction tomography (IDT) technique based on a standard microscope modified with an annular LED illumination hardware unit. Our label-free imaging method enables *in vitro* biological sample observation providing intrinsic 3D structural RI sensitivity of large volumes at real-time acquisition speeds.

Due to the low absorption and contrast of biological samples in the visible spectrum, exogenous labels (e.g. fluorophores) are commonly used as biomarkers to visualize regions of interest. For example, confocal fluorescence and two-photon microscopy are commonly used when imaging thick 3D samples. Although these methods provide excellent optical sectioning, the excitation light and contrast agents for fluorescence imaging can cause photobleaching, phototoxicity, and other damaging effects that artificially alter the sample’s behavior and structure [3]. These factors have pushed the need for label-free microscopy, where biological samples are studied in their natural states. Quantitative phase imaging (QPI) [1, 4] is one such technique that measures an incident field’s phase shifts induced by the sample to recover the sample’s physical properties without staining or labeling. Both interferometry [5–8] and non-interferometry based [9–12] QPI techniques have been developed to recover a sample’s phase map in two-dimensions (2D). A single 2D integrated phase image, however, is insufficient for characterizing 3D heterogeneous samples. Recently developed 3D phase tomography techniques instead recover the sample’s 3D RI distribution to visualize intracellular structures [13–15].

The most widely used interferometry-based RI tomography technique is optical diffraction tomography (ODT). In ODT, the scattered field is directly measured from digitally recorded interferograms taken under different illumination angles (i.e. phase projection measurement). Several ODT approaches have been applied in biomedical studies for evaluating cell physiology [16, 17], pathophysiology and immunology [18–21], oncology [22–24], and micro-organism and intracellular particle tracking [25, 26]. Notably, annular illumination is particularly effective in achieving high-quality 3D RI recovery using a relatively small number of phase projection measurements. The phase nanoscopy technique [14] allows both static and time-lapse 3D RI recovery of cells by mechanically scanning a laser illumination unit along a ring-shaped trajectory. An alternative ODT microscope builds on a programmable illumination unit using a digital micromirror device (DMD) to generate plane wave illumination with annularly distributed angles [27, 28]. However, both techniques require additional optical paths

for off-axis or common-path interferometric recording that are difficult to implement in existing microscope platforms.

Here, we demonstrate a technique simplifying the hardware requirement for RI tomography using *intensity-only, non-interferometry* based measurements. Our method is based on the principle of IDT [29] and is implemented on a standard brightfield microscope equipped with a programmable LED ring. Existing IDT techniques often require sample or objective scanning along the axial direction to capture a through-focus intensity stack [30–32]. The 3D RI map is then recovered using deconvolution algorithms [33, 34]. For example, the gradient light interference microscopy [15] achieves 3D imaging of thick biological samples using a DIC through-focus intensity stack. The 3D differential phase contrast microscopy approach takes an axially-scanned intensity stack under asymmetric partially coherent illumination [34]. However, the mechanical motion limits the acquisition speed for a single measurement to several minutes. Recently, *motion-free* IDT techniques have been demonstrated by our group allowing 3D RI information recovery using oblique illumination-only intensity measurements *without* any mechanical scanning. Our original illumination-based IDT technique is limited by its large data requirement (requiring more than 600 images per volume) [29], which is not suited for imaging live biological samples and suffers from severe motion artifacts from dynamic samples.

Here, we develop a fast and accurate annular illumination IDT (aIDT) technique overcoming these limitations. Importantly, our technique reduces the data requirement by more than $60\times$, achieving more than 10Hz for imaging a $\sim 350 \times 100 \times 20\mu\text{m}^3$ volume with near diffraction-limited lateral resolution of 487 nm and axial resolution of $3.4 \mu\text{m}$ in the 3D RI reconstruction. These improvements enable *in vitro* dynamic 3D RI characterizations of living biological samples. We show that our technique provides useful subcellular information on multiple species including unicellular diatom microalgae, clustered epithelial buccal cells, and live *Caenorhabditis elegans* (*C. elegans*) multi-cellular specimens.

Our technique is enabled by several hardware and algorithmic innovations. First, our hardware employs a programmable LED ring consisting of only 24 surface-mounted LEDs. Compared to existing LED matrix based systems [34–40], the reduced number of LEDs significantly speed up the acquisition. More importantly, the ring illumination geometry can optimally fit with the circular microscope pupil, which we show is crucial for both data reduction and high-quality RI reconstruction. We develop an illumination-based IDT theory that highlights the optimal imaging condition achieved by matching the illumination angle with the objective numerical aperture (NA). This illumination scheme optimally encodes both low and high spatial frequency RI information across the entire 3D volume using a small number of intensity measurements. This allows us to use only 8 intensity measurements for imaging fast dynamics and provides an optimal trade-off between RI reconstruction quality and motion artifacts. We develop a new reconstruction algorithm that implement a non-iterative slice-wise

deconvolution that is both data and computationally efficient. We further develop a robust self-calibration algorithm to correct for the LED positions, which we show is critical for high-quantity 3D RI reconstruction, in particular at large defocus positions.

2 Results

2.1 aIDT principle

Our aIDT imaging system combines an LED ring illumination unit and a standard brightfield microscope (Fig. 1a). The LED ring is placed some distance h away under the sample, as illustrated in Fig. 1b. Importantly, the distance is carefully tuned such that the ring is matched with the perimeter of the objective lens’s pupil aperture. This can be done because this illumination design approximately follows the Köhler geometry, in which each LED provides a plane wave of unique angle. Denoting the radius of the ring as r , the illumination NA (NA_{illum}) of each LED is set by $\text{NA}_{\text{illum}} = r/\sqrt{r^2 + h^2}$. Hence, one can achieve NA_{illum} matching the objective NA (i.e. $\text{NA}_{\text{obj}} = \text{NA}_{\text{illum}}$) by simply adjusting the LED height h . During the experiment, we acquire up to 24 images capturing brightfield intensity measurements from each individual LED in our ring unit (Fig. 1c). By downsampling the total LED number, we can reduce our acquisition speed to accommodate dynamic live samples.

The intensity of each image results from the interference of the scattered field from the object and the unperturbed illuminating field (Fig. 1c). By quantifying the Fourier space information under the first Born approximation, we derive phase and absorption transfer functions (TFs) [29] *linearly* relating the object’s complex permittivity distribution to the measured intensity. The exact form of the TFs are detailed in Eqs. (1–2) in Sec. 4.2. The TFs are angle and depth-dependent and result in the 4D Fourier space representation shown in Fig. 1d. This relation allows us to implement a fast and efficient slice-wise 3D deconvolution algorithm with a closed form solution (Eq. S1 in Supplementary Information) to recover the complex 3D RI distribution.

Several important observations govern our illumination design. First, each TF’s Fourier coverage features a pair of circular regions describing the scattered field’s information and its complex conjugate. The system’s objective NA_{obj} defines the circles’ radius while the illumination angle NA_{illum} defines the center positions. By matching NA_{illum} to NA_{obj} , one ensures maximum Fourier coverage allowed by the system (i.e. 2NA_{obj}), as demonstrated in Fig. S1 in Supplementary Information. Second, the phase information is captured by the *anti-symmetric* Fourier information whereas the absorption information is by the *symmetric* part (Fig. 1d). The antisymmetry in the phase TF further indicates that any overlap between the two circular regions (by

using $\text{NA}_{\text{illum}} < \text{NA}_{\text{obj}}$) results in cancellation in the captured low spatial frequency information. By setting $\text{NA}_{\text{illum}} = \text{NA}_{\text{obj}}$, it removes the overlap and ensures optimal low frequency phase information coverage. Together, our annular illumination scheme enables capturing both high and low spatial frequency phase and absorption information in 3D using a small number of intensity-only measurements.

2.2 Angle self-calibration and performance characterization

Achieving high-quality RI tomographic reconstruction requires accurate LED positioning, especially when imaging large-volume objects under high NA illuminations. In practice, removing all residual errors in the LED positions using only manual alignment and physical calibration procedures is non-trivial. We instead develop an algorithmic self-calibration method for finely tuning the LED positions and demonstrate our technique’s improvement of 3D reconstructions.

Our self-calibration method combines two main principles for high-accuracy measurements. First, our TF analysis shows that each intensity image’s Fourier spectrum should contain distinct circular regions with center positions defining the illumination angle. A demonstration of this principle on experimental data is shown in the Supplementary Movie S1. The algorithm in [41] already utilizes these features, so we adopted this technique to provide initial LED position estimates. In practice, this algorithm’s susceptibility to noise can introduce position error exceeding the illumination unit’s engineering and alignment tolerance. To correct this error, we subsequently incorporate two geometric constraints refining the LED positions to form a ring shape with equal angular spacing using a nonlinear fitting algorithm. This is warranted because the surface-mount technology has high position accuracy of device placement in printed circuit board manufacture process and our illumination unit’s printed LED circuits have expected engineering tolerances below $5\mu\text{m}$ generally. More details about this algorithm are presented in Sec. 4.3.

We demonstrate the effectiveness of this method on diatom microalgae (S68786, Fisher Scientific) fixed in glycerine gelatin imaged with a 0.65 NA objective lens. An example intensity image is shown in Fig. 2a. The low-absorbing features (i.e. “phase” features) are already visible due to asymmetric illumination, akin to differential phase contrast [42]. Figure 2b compares the LED positions from manual alignment (blue stars) and our self-calibration method (green triangles) (More details are illustrated in Fig. S2 in Supplementary Information). The RI reconstruction improvements from our technique are shown in three insets highlighting features located at different axial positions.

As shown in Fig. 2d, the LED mis-calibrations have minimal effect for structure reconstructions at the objective’s focal plane ($z = 0\mu\text{m}$). Significant RI degradation from incorrect illumination angles is observed at defocus reconstruction planes (Fig. 2c,e). This degradation is intuitively explained under the “light field” ef-

fect [38,39]: for a fixed angular error, a larger defocus induces a larger feature displacement error. Our self-calibration method largely mitigates these errors to provide high-quality RI reconstructions (Fig. 2c-e). Both the lateral resolution and contrast are preserved across the entire volume and recovers diatom frustules previously lost at large defocus due to mis-calibration (Fig. 2e). This calibration procedure allow us to provide high-quality RI distributions with aIDT and is used in our subsequent results.

2.3 Tomographic characterization of *Surirella spiralis*

We demonstrate aIDT’s ability to characterize complex single cell organisms with intracellular resolution on a *Surirella spiralis* diatom sample. We acquired 24 intensity images under oblique illuminations and reconstructed the sample’s RI across a 50 μm volume as shown in Fig. 3. The benefit of this technique is clearly shown in its recovery of multi-scale features of the sample. aIDT recovers the characteristic *Surirella spiralis* saddle shape spanning the full 50 μm reconstructed volume (Fig. 3a-c). Within this large saddle, fine structures including silica frustules are also visible and well-resolved across multiple reconstructed slices (Fig. 3d,f-h). Line profiles across these 10 μm tall frustules in Fig. 3j-l demonstrate near diffraction-limited lateral resolution of 487 nm and axial resolution of 3.4 μm .

aIDT quantitatively recovers both full cell-sized features and intracellular structures easily using a small set of intensity images from a single focal plane. These results make aIDT advantageous for biological research applications containing complex environments requiring simultaneous, multi-scale sample evaluation. In addition, the lack of sample scanning with this technique increases its utility for dynamic sample imaging where living objects easily move out-of-focus. We show aIDT’s application to both of these cases in the subsequent sections.

2.4 RI tomography on cell clusters

We next apply aIDT to evaluating complex biological cell clusters and environments. Existing 2D phase imaging techniques are often used when imaging monolayers of cells. These integrated phase map techniques contain less useful information, however, when imaging cell clusters more commonly found in biological systems. Our aIDT technique overcomes this problem by recovering multiple, independent RI cross-sections across extended volumes. This approach enables better depth-sectioning of the sample such that larger biological structures with greater complexity can be evaluated without significant information loss.

We demonstrate this ability to recover complex biological environments on clusters of unstained human epithelial buccal cells distributed on a glass sample slide. A sample normalized intensity image is shown in Fig. 4a showing the cell cluster’s

complexity and its defocused regions highlighting the sample’s large volume. We take 24 intensity images and reconstruct the RI across a 16 μm volume. We expand two regions of the reconstructed RI in Fig. 4b,c highlighting our depth-sectioned reconstructions.

The benefit of aIDT when imaging complex environments is seen in its high-resolution reconstructions across the entire cell volume. At each reconstructed slice we observe cellular membrane folds, cell boundaries, nuclei, and intracellular features with high resolution (Fig. 4b,c arrows). In addition, we recover native bacteria, likely a staphylococcus strain, distributed on the cells throughout the sample (Fig. 4b,c circles).

Quantifying the 3D RI distribution of entire cells, their subcellular structures, and external environment features such as bacteria has significant potential in biological research applications. The recovered volumetric RI distributions of cellular features enables the calculation of dry and bouyant mass, sphericity, and other morphometric descriptors used for cell profiling [43,44]. Because subcellular and bacterial structures are also resolved, these parameters can be applied to subcellular features with aIDT. With aIDT’s fast acquisition rates and large volume recovery, shown experimentally in the next section, longitudinal maps of structure mass and volume changes can be mapped in real-time throughout multi-cellular complex environments. Quantifying these factors could be highly beneficial to immunology and pathophysiology applications ,where longitudinal studies of parasite and bacterial interactions and induced morphological changes in cells carry critical information for understanding and mitigating infection [18,45]. Furthermore, quantifying volumetric morphological changes of cellular and subcellular information also has significant utility in oncology for both differentiating cancer types and evaluating their response to drug and therapy treatments [22–24].

2.5 Dynamic RI tomography of *C. elegans* in vitro

A major advancement enabled by aIDT is the ability to perform high-speed *in vitro* tomographic imaging of biological samples using a small number of intensity-only measurements. This allows us to visualize 3D dynamical biological phenomena with minimal motion artifacts, which is particularly challenging using existing RI tomography techniques. We demonstrate this ability on unstained, live *C. elegans* worms at a 10.6 Hz volume rate. We image a volume containing $333 \times 98 \times 21 \mu\text{m}^3$. In a time-lapse series, each image stack includes 8 frame (for reconstructing each RI volume) is recorded with a 4.4 ms exposures time over a 3 min period to evaluate fast motions in a living *C. elegans*.

The reconstructed RI of the *C. elegans* worm is shown in Fig. 5. Reconstructed RI $x - y$ and $x - z$ cross-sections at the $z = 0\mu\text{m}$ plane at $t = 0$ sec are shown in Fig. 5a and Fig. 5b, respectively. Fig. 5c shows the RI distribution of worm at

different z planes in the marked region at $t = 0$ sec. And Fig. 5d illustrates the RI distribution of the *C. elegans* internal tissue structures at different time points and axial planes. Depth-coded projections of our reconstructions are also provided in Fig. 5e, where the volumetric RI distribution is shown for several different time points. The full *C. elegans* worm reconstruction video is shown in Supplementary Movie S6. This approach is robust to motion artifacts and still resolves internal features during high-speed worm motion as clearly demonstrated in the Supplementary Movie S7.

Our technique easily visualizes and provides RI quantification of the *C. elegans* internal tissues. The anterior and terminal pharyngeal bulbs are clearly resolved in our reconstruction (Fig. 5a,c) as well as the grinder and intestines (Fig. 5c circles, Fig. 5d long bracket). Lipid droplets and lysosomes are also distinguished in the worm head at different axial layers (Fig. 5c arrows). Within the worm body, we recover the vulva (Fig. 5d circles) across multiple axial slices, body wall muscles (Fig. 5d short brackets), and features resembling the worm’s nerve cord (Fig. 5d). We also observe *E. coli* bacteria living and moving independently of the *C. elegans* (Fig. 5d small circles). More details about the 3D results of fixed *C. elegans* can be found in Supplementary Information and Movie S8.

aIDT enables a simple, label-free approach for volumetric imaging in the biological research community. The tissues shown in Fig. 5 and Movie S6 often undergo phenotypic changes from genetic mutations during biological studies [46]. Quantifying these tissue changes and studying their effect on live worm behavior in a natural, label-free setting would be highly beneficial in understanding the effects of targeted genetic mutations on living organisms. Because our technique captures bacteria motion concurrently with the *C. elegans*, aIDT could also evaluate multi-organism interactions and provide 3D bacteria tracking during longitudinal studies. The versatility of this technique in visualizing multiple tissue types means it has utility spanning from neurology to pathogenesis and wound healing [46].

3 Discussion

We introduced aIDT, a high-speed, label-free, scanless non-interferometry based quantitative imaging tool for the 3D evaluation of unlabeled specimens. By combining an LED ring illumination unit with a standard brightfield microscope, we capture obliquely illuminated intensity images and perform 3D deconvolution to recover the slice-wise 3D RI distribution. The geometry fitting between illumination angle with the objective NA optimally encodes both low and high spatial frequency into each acquired image. This illumination scheme reduces the system’s data requirement and allows us to image large 3D volume of thick samples at high speeds. We demonstrated the success of aIDT on various biological samples, from fixed microalga, cheek cells, to living *C. elegans*. We believe that this method will set an excellent foundation

for other research projects and applications, and the aIDT has the potential as a tool of great biological interest by showing its use in monitoring cell morphology and dynamics in noninvasive high-speed measurements.

4 Materials and methods

4.1 System setup

Our aIDT setup is built on an upright brightfield microscope (TE200, Nikon) and replaces the existing illumination unit with a ring LED (Product number 1586, Adafruit). The radius of ring LED unit is ~ 30 mm. The LED ring is placed ~ 35 mm away from the sample, whose center is aligned with the optical axis of the microscope. Each LED approximately provides spatially coherent quasi-monochromatic illumination with central wavelength $\lambda = 515$ nm, and ~ 20 nm bandwidth. All experiments in the main text were conducted using a $40\times$ microscope objective (MO) (0.65 NA, CFI Plan Achromatic). Images were taken with an sCMOS camera (PCO. Panda 4.2, $6.5\mu\text{m}$ pixel size), which is synchronized with the LED source to provide camera limited acquisition speed. The LED ring unit is driven by a micro-controller (Arduino Uno, Arduino). In addition, we provide additional results using a $10\times$ (0.25 NA, CFI Plan Achromatic) MO to image spiral algae (S68786, Fisher Scientific) in Supplementary Information. During the experiments of imaging living *C. elegans*, a rectangular field of view consisting of 2048×600 pixels is optimized to achieve 85Hz acquisition speed.

4.2 Data processing for IDT imaging

In the aIDT forward model, a 3D sample is discretized into a stack of 2D sample slices. Following the derivation in [29], the 3D phase and absorption TFs can be derived slice-by-slice and as a function of the illumination angle. The analytical expression of the phase TF (H_P) and absorption TF (H_A) can be expressed as

$$H_P(\mathbf{u}) = |P(\mathbf{u} - \rho_s)| \cos \left[kz \left(\sqrt{1 - \lambda^2 |\mathbf{u} - \rho_s|^2} - \sqrt{1 - \lambda^2 |\rho_s|^2} \right) \right] - |P(\mathbf{u} + \rho_s)| \cos \left[kz \left(\sqrt{1 - \lambda^2 |\mathbf{u} + \rho_s|^2} - \sqrt{1 - \lambda^2 |\rho_s|^2} \right) \right] \quad (1)$$

and

$$H_A(\mathbf{u}) = |P(\mathbf{u} - \rho_s)| \cos \left[kz \left(\sqrt{1 - \lambda^2 |\mathbf{u} - \rho_s|^2} - \sqrt{1 - \lambda^2 |\rho_s|^2} \right) \right] + |P(\mathbf{u} + \rho_s)| \cos \left[kz \left(\sqrt{1 - \lambda^2 |\mathbf{u} + \rho_s|^2} - \sqrt{1 - \lambda^2 |\rho_s|^2} \right) \right], \quad (2)$$

respectively, where ρ_s denotes the spatial frequency of the illumination, \mathbf{u} the 2D spatial frequency variable, P the pupil function of the MO, $k = 2\pi/\lambda$ the wave number, λ the illumination wavelength, z the sample axial location.

Next, the 3D RI reconstruction is achieved by solving an inverse problem by a deconvolution procedure (more details about data processing see Supplementary Methods). Importantly, since the TFs are slice-wise – the information from different sample slices are *decoupled* from each other. This allows us to use a highly computationally efficient slice-based deconvolution procedure to reconstruct the cross-sectional RI distribution one slice at a time. The slice spacing can be chosen arbitrarily during the computation. The achieved axial resolution is characterized by analyzing the reconstructed stack and is found to approximately match with the diffraction limit, set by $\lambda/(n_m - \sqrt{n_m^2 - \text{NA}_{\text{obj}}^2})$, where n_m is the RI of surrounding medium.

All the processing is done using MATLAB on a personal computer. The processing time to perform LED position calibration (for $400 \times 400 \times 24$) is about 2 seconds. 3D reconstruction time for a $1024 \times 1024 \times 51$ RI stack takes about 50 seconds.

4.3 Self-calibration method

During the reconstruction, we first perform a numerical self-calibration procedure. The algorithm follows two geometric constraints. First, the distribution of our LED ring is expected to obey a circular geometry as

$$u_i^2 + v_i^2 = (\text{NA}_{\text{obj}}/\lambda)^2, \quad (3)$$

where (u_i, v_i) denote the initial estimated spatial frequency for the i th LED. Second, the LEDs are expected to be equally spaced. Correspondingly, each pair of neighboring LEDs occupy a $\pi/12$ radian angular space. The initial estimate of the angular coordinates θ_i of each LED follows

$$\theta_i = \text{atan2}(v_i/u_i), \text{ and } \theta_i \in \left[-\pi : \frac{\pi}{12} : \pi\right) \quad (4)$$

Our self-calibration algorithm starts with an initial guess $u_i^{\text{init}}, v_i^{\text{init}}$ from the algorithm in [41], whose estimated LED positions are often contaminated by noise. Accordingly, the final calibrated LED positions $u_i^{\text{cal}}, v_i^{\text{cal}}$ are parameterized as

$$\begin{aligned} u_i^{\text{cal}} &= \Delta u + \text{NA}_{\text{obj}} \cos(\theta_i + \Delta\theta) / \lambda \\ v_i^{\text{cal}} &= \Delta v + \text{NA}_{\text{obj}} \sin(\theta_i + \Delta\theta) / \lambda, \end{aligned} \quad (5)$$

and are found by solving the optimization problem

$$\min_{u_i^{\text{cal}}, v_i^{\text{cal}}} \sum_{i=1}^{24} (v_i^{\text{cal}} - u_i^{\text{init}})^2 + (v_i^{\text{cal}} - v_i^{\text{init}})^2. \quad (6)$$

4.4 Sample preparation

For buccal smear, the fresh human buccal epithelial cells are placed in the gap between the coverslips and glass slide with 0.9% sodium chloride matching solution ($n_m = 1.33$). For *C. elegans* preparation, the worms were mounted on 3% agarose pads in a drop of nematode growth medium (NGM) buffer. A solid pad was made with 3% agarose in NGM buffer and placed onto the slide. Then a drop of liquid NGM buffer was applied on top of the agarose pad, and young adult *C. elegans* were added to this liquid drop. Glass coverslips were then gently placed on top of the pads and sealed with a 1:1 mixture of paraffin and petroleum jelly [47, 48]. The RI of liquid NGM buffer medium inside slit is 1.33, which is similar to water due to low salt concentrations.

4.5 Data and code availability

The Matlab codes and raw experimental data in this manuscript are available on GitHub at <https://github.com/bu-cisl/IDT-using-Annular-Illumination>.

References

- [1] Park, Y., Depeursinge, C. & Popescu, G. Quantitative phase imaging in biomedicine. *Nat. Photon.* **12**, 578 (2018).
- [2] Merola, F. *et al.* Tomographic flow cytometry by digital holography. *Light Sci. Appl.* **6**, e16241 (2017).
- [3] Stephens, D. J. & Allan, V. J. Light microscopy techniques for live cell imaging. *Science* **300**, 82–86 (2003).
- [4] Popescu, G. *Quantitative phase imaging of cells and tissues* (McGraw Hill Professional, 2011).
- [5] Kemper, B. & Von Bally, G. Digital holographic microscopy for live cell applications and technical inspection. *Appl. Opt.* **47**, A52–A61 (2008).
- [6] Ferraro, P. *et al.* Quantitative phase-contrast microscopy by a lateral shear approach to digital holographic image reconstruction. *Opt. Lett.* **31**, 1405–1407 (2006).
- [7] Wang, Z. *et al.* Spatial light interference microscopy (SLIM). *Opt. Express* **19**, 1016–1026 (2011).
- [8] Baek, Y., Lee, K., Shin, S. & Park, Y. Kramers–kronig holographic imaging for high-space-bandwidth product. *Optica* **6**, 45–51 (2019).

- [9] Waller, L., Tian, L. & Barbastathis, G. Transport of intensity phase-amplitude imaging with higher order intensity derivatives. *Opt. Express* **18**, 12552–12561 (2010).
- [10] Alieva, J. A. R. T. Rapid Quantitative Phase Imaging for Partially Coherent Light Microscopy. *Opt. Express* **22**, 13472–13483 (2014).
- [11] Tian, L. & Waller, L. Quantitative differential phase contrast imaging in an LED array microscope. *Opt. Express* **23**, 11394–11403 (2015).
- [12] Zuo, C. *et al.* High-resolution transport-of-intensity quantitative phase microscopy with annular illumination. *Sci. Rep.* **7**, 7654 (2017).
- [13] Choi, W. *et al.* Tomographic phase microscopy. *Nat. Methods* **4**, 717–719 (2007).
- [14] Cotte, Y. *et al.* Marker-free phase nanoscopy. *Nat. Photon.* **7**, 113–117 (2013).
- [15] Nguyen, T. H., Kandel, M. E., Rubessa, M., Wheeler, M. B. & Popescu, G. Gradient light interference microscopy for 3D imaging of unlabeled specimens. *Nat. Commun.* **8**, 210 (2017).
- [16] Sung, Y. *et al.* Optical diffraction tomography for high resolution live cell imaging. *Opt. Express* **17**, 266–277 (2009).
- [17] Kuś, A., Dudek, M., Kemper, B., Kujawińska, M. & Vollmer, A. Tomographic phase microscopy of living three-dimensional cell cultures. *J. Biomed. Opt.* **19**, 046009–046009 (2014).
- [18] Chandramohanadas, R. *et al.* Biophysics of malarial parasite exit from infected erythrocytes. *PLoS ONE* **6**, e20869 (2011).
- [19] Yoon, J. *et al.* Label-free characterization of white blood cells by measuring 3d refractive index maps. *Biomed. Opt. Express* **6**, 3865–3875 (2015).
- [20] Lee, K. *et al.* Quantitative phase imaging techniques for the study of cell pathophysiology: from principles to applications. *Sensors* **13**, 4170–4191 (2013).
- [21] Yakimovich, A., Witte, R., Andriasyan, V., Georgi, F. & Greber, U. F. Label-free digital holo-tomographic microscopy reveals virus-induced cytopathic effects in live cells. *mSphere* **3**, e00599–18 (2018).
- [22] Sung, Y., Choi, W., Lue, N., Dasari, R. R. & Yaqoob, Z. Stain-free quantification of chromosomes in live cells using regularized tomographic phase microscopy. *PLoS ONE* **7**, e49502 (2012).

- [23] Li, Y., Fanous, M. J., Kilian, K. A. & Popescu, G. Quantitative phase imaging reveals matrix stiffness-dependent growth and migration of cancer cells. *Sci. Rep.* **9**, 248 (2019).
- [24] Zhikhoreva, A. *et al.* Morphological changes in the ovarian carcinoma cells of wistar rats induced by chemotherapy with cisplatin and dioxadet. *Biomed. Opt. Express* **9**, 5817–5827 (2018).
- [25] Isikman, S. O. *et al.* Lens-free optical tomographic microscope with a large imaging volume on a chip. *Proc. Natl. Acad. Sci. USA* **108**, 7296–7301 (2011).
- [26] Kim, D. *et al.* Label-free high-resolution 3-d imaging of gold nanoparticles inside live cells using optical diffraction tomography. *Methods* **136**, 160–167 (2018).
- [27] Shin, S., Kim, K., Yoon, J. & Park, Y. Active illumination using a digital micromirror device for quantitative phase imaging. *Opt. Lett.* **40**, 5407–5410 (2015).
- [28] Shin, S., Kim, D., Kim, K. & Park, Y. Super-resolution three-dimensional fluorescence and optical diffraction tomography of live cells using structured illumination generated by a digital micromirror device. *Sci. Rep.* **8** (2018).
- [29] Ling, R., Tahir, W., Lin, H.-Y., Lee, H. & Tian, L. High-throughput intensity diffraction tomography with a computational microscope. *Biomed. Opt. Express* **9**, 2130–2141 (2018).
- [30] Soto, J. M., Rodrigo, J. A. & Alieva, T. Label-free quantitative 3d tomographic imaging for partially coherent light microscopy. *Biomed. Opt. Express* **25**, 15699–15712 (2017).
- [31] Rodrigo, J. A., Soto, J. M. & Alieva, T. Fast label-free microscopy technique for 3d dynamic quantitative imaging of living cells. *Biomed. Opt. Express* **8**, 5507–5517 (2017).
- [32] Li, J. *et al.* Three-dimensional tomographic microscopy technique with multi-frequency combination with partially coherent illuminations. *Biomed. Opt. Express* **9**, 2526–2542 (2018).
- [33] Jenkins, M. H. & Gaylord, T. K. Three-dimensional quantitative phase imaging via tomographic deconvolution phase microscopy. *Appl. Opt.* **54**, 9213–9227 (2015).
- [34] Chen, M., Tian, L. & Waller, L. 3D differential phase contrast microscopy. *Biomed. Opt. Express* **7**, 3940–3950 (2016).

- [35] Zheng, G., Horstmeyer, R. & Yang, C. Wide-field, high-resolution Fourier Ptychographic microscopy. *Nat. Photon.* **7**, 739–745 (2013).
- [36] Horstmeyer, R., Chung, J., Ou, X., Zheng, G. & Yang, C. Diffraction tomography with fourier ptychography. *Optica* **3**, 827–835 (2016).
- [37] Tian, L. *et al.* Computational illumination for high-speed in vitro Fourier ptychographic microscopy. *Optica* **2**, 904–911 (2015).
- [38] Tian, L. & Waller, L. 3D intensity and phase imaging from light field measurements in an LED array microscope. *Optica* **2**, 104–111 (2015).
- [39] Tian, L., Wang, J. & Waller, L. 3D differential phase-contrast microscopy with computational illumination using an LED array. *Opt. Lett.* **39**, 1326–1329 (2014).
- [40] Tian, L., Li, X., Ramchandran, K. & Waller, L. Multiplexed coded illumination for Fourier ptychography with an LED array microscope. *Biomed. Opt. Express* **5**, 2376–2389 (2014).
- [41] Eckert, R., Phillips, Z. F. & Waller, L. Efficient illumination angle self-calibration in fourier ptychography. *Appl. Opt.* **57**, 5434 (2018).
- [42] Mehta, S. & Sheppard, C. Quantitative phase-gradient imaging at high resolution with asymmetric illumination-based differential phase contrast. *Opt. Lett.* **34**, 1924–1926 (2009).
- [43] Lobo, J., See, E. Y.-S., Biggs, M. & Pandit, A. An insight into morphometric descriptors of cell shape that pertain to regenerative medicine. *J. Tissue Eng. Regen. Medicine* **10**, 539–553 (2016).
- [44] Zangle, T. A. & Teitell, M. A. Live-cell mass profiling: an emerging approach in quantitative biophysics. *Nat. Methods* **11**, 1221 (2014).
- [45] Sadrearhami, Z. *et al.* Antibiofilm nitric oxide releasing polydopamine coatings. *ACS Appl. Mater. Interfaces* (2019).
- [46] Corsi, A. K., Wightman, B. & Chalfie, M. A transparent window into biology: a primer on caenorhabditis elegans. *Genetics* **200**, 387–407 (2015).
- [47] Stiernagle, T. Maintenance of *c. elegans*. wormbook. the *c. elegans* research community. *WormBook* (2006).
- [48] Kim, E., Sun, L., Gabel, C. V. & Fang-Yen, C. Long-term imaging of caenorhabditis elegans using nanoparticle-mediated immobilization. *PLoS ONE* **8**, e53419 (2013).

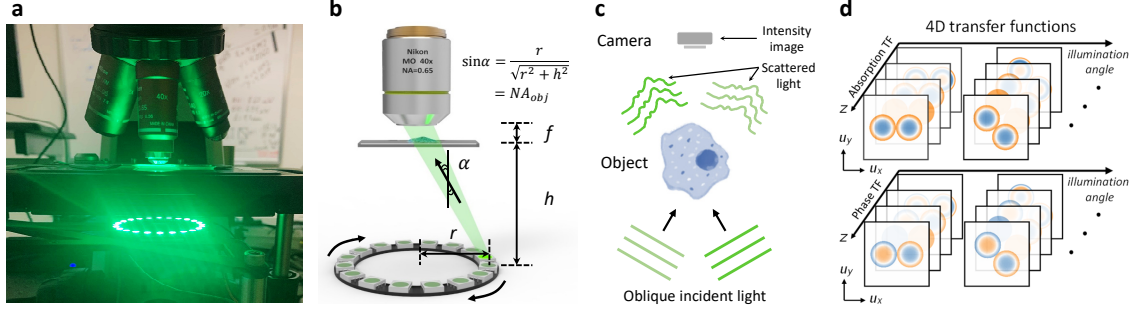


Figure 1: Illustration of our aIDT imaging system. (a) A photo of our aIDT system consisting of a standard microscope equipped with an LED ring. A video demonstrating the operation of the system is shown in Supplementary Movie S1. (b) An LED ring illumination unit is placed underneath the sample. The distance h is tuned such that the illumination angle α is matched with the objective NA. (c) Each IDT image measures the interference between the scattered and the unperturbed fields. (d) The absorption and phase transfer functions at various illumination angles and sample depths.

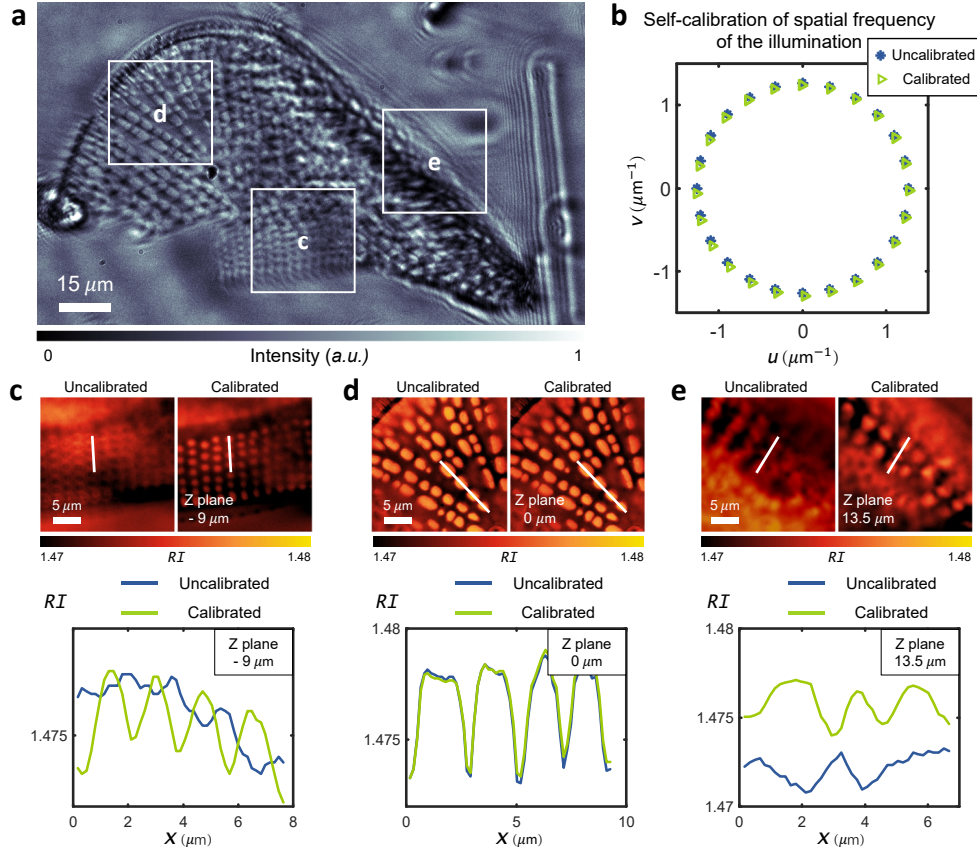


Figure 2: Results from our LED position self-calibration method. (a) A sample intensity image of a diatom under a certain single-LED illumination. (b) LED positions from manual alignment (termed uncalibrated, marked in blue star) and our self-calibration methods (termed calibrated, marked in green triangle) as plotted in the spatial frequency coordinates. (c-e) Comparison of the reconstructed RI slides before and after calibration. (c) $z = -9\mu\text{m}$, (d) $z = 0\mu\text{m}$, and (e) $z = 13.5\mu\text{m}$. More detailed comparisons across the whole volume is provided in Supplementary Movie S3.

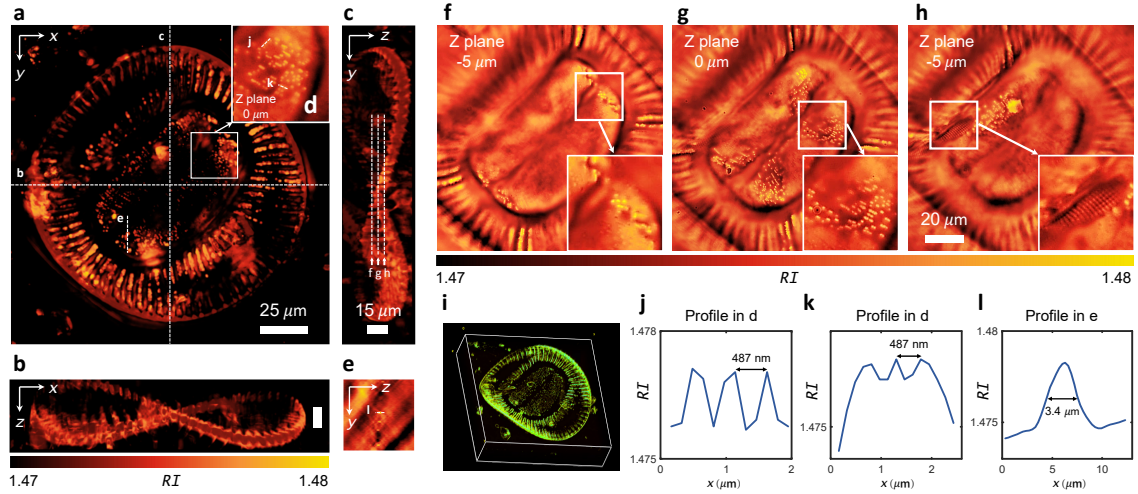


Figure 3: RI tomography of *Surirella spiralis*. (a-c) The maximum RI projection views of the recovered 3D RI distribution in the $x-y$, $x-z$, and $y-z$ planes. (d,e) Zoom-in on closely packed frustule structures. (f-h) Reconstructed 2D cross sectional RI slices at $-5 \mu\text{m}$, $0 \mu\text{m}$ and $5 \mu\text{m}$ planes. (i) A 3D rendering view of the reconstructed RI distribution. Additional cross-sectional reconstruction and 3D rendering view from different perspectives are shown in Supplementary Movie S4. (j-l) Line profiles across frustule structures to quantify the reconstructed lateral and axial resolution.

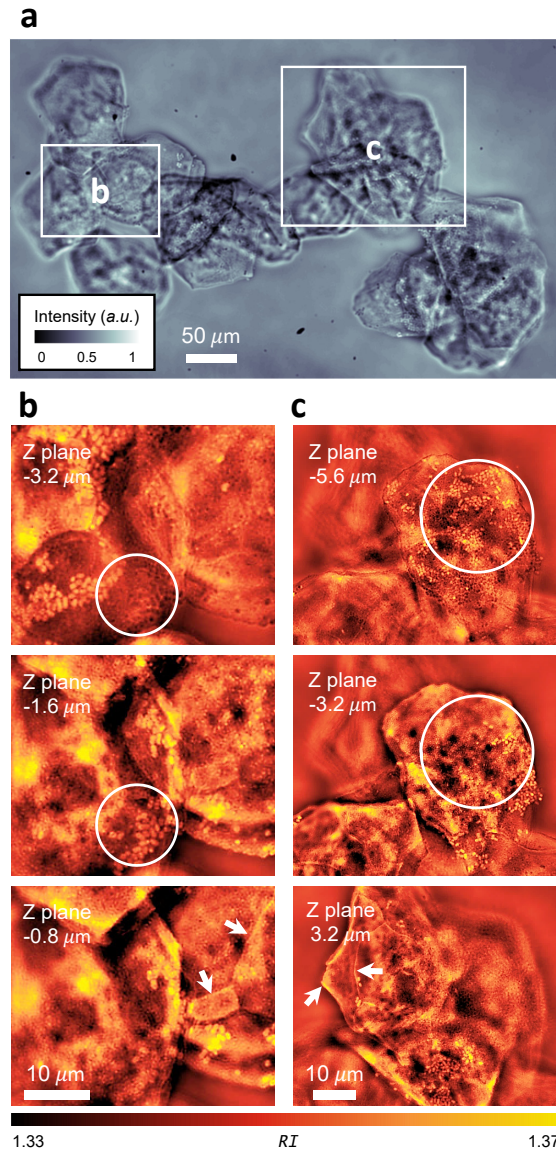


Figure 4: Single cell RI tomography of unstained human cheek cell clusters. (a) A sample raw intensity image under annular illumination. (b,c) Reconstructed RI cross-sections demonstrate the sectioning capability enabled by the aIDT. Additional examples are shown in Supplementary Movie S5.

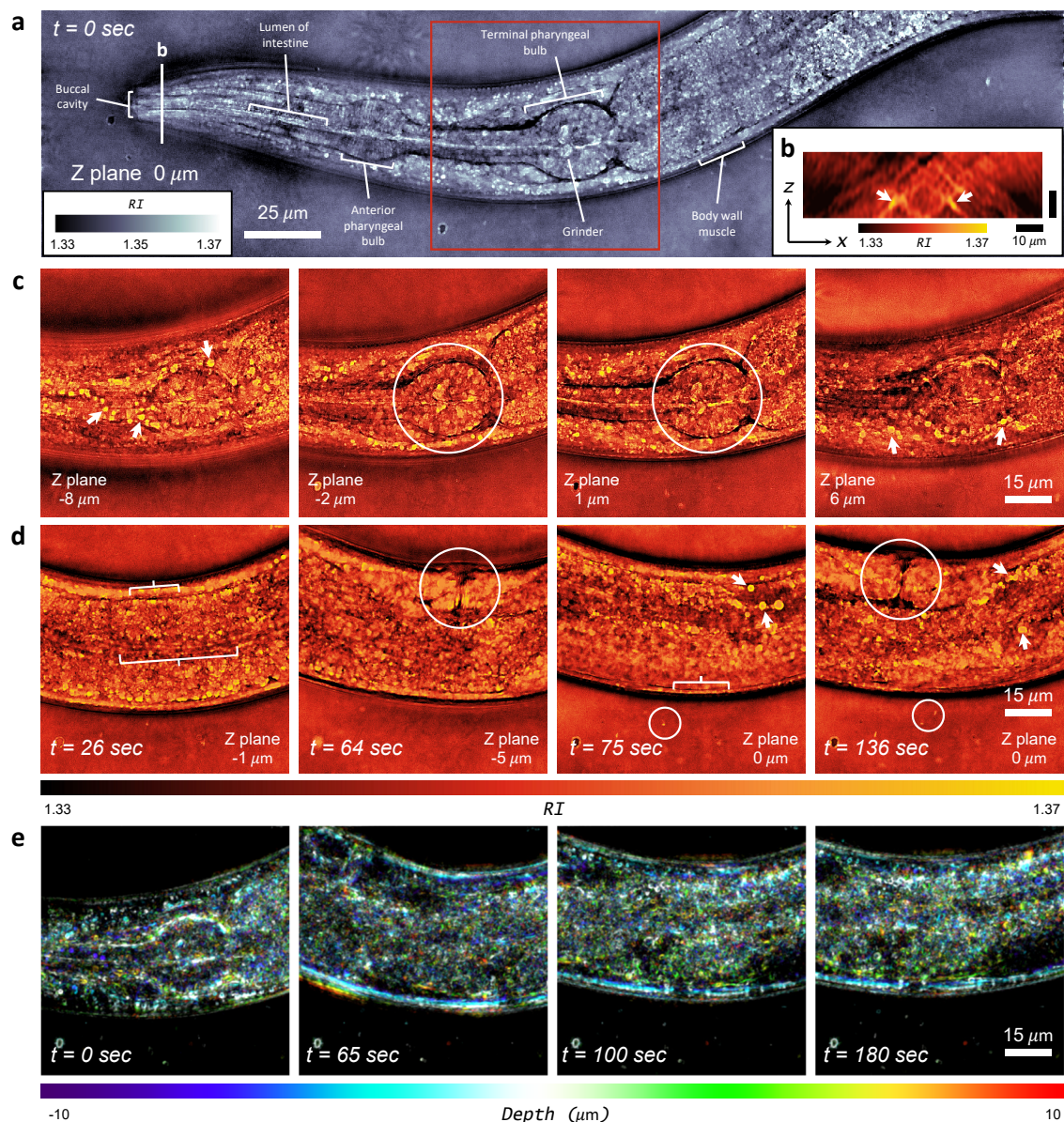


Figure 5: Time-lapse *in vitro* tomographic imaging of *C. elegans*. (a) Recovered RI slice located at central plane at $t = 0$ sec. The full *C. elegans* worm reconstruction video is shown in Supplementary Movie S6. (b) RI stack section in $x - z$ plane close to the mouth of *C. elegans*. Buccal cavity of *C. elegans* is distinguishable (indicated by the white arrows). (c) RI distribution of worm at different z planes in the marked red square region at $t = 0$ sec. Time-lapse details are demonstrated in Supplementary Movie S7. (d) Visualizations and RI quantification of the *C. elegans* internal tissue structures at different time points and axial planes. (e) Depth color coding of 3D RI measurements of sample in the selected sub-region with fix position in the field of view. 4 different time points to illustrate the time lapse results of *C. elegans*.